Article

Time-Domain Topology Optimization of Arbitrary Dispersive Materials for Broadband 3D Nanophotonics Inverse Design

Johannes Gedeon,* Emadeldeen Hassan,* and Antonio Calà Lesina*

Read Online

ACCESS | Metrics & More | Article Recommendations | Supporting Information

ABSTRACT: In the last decades, nanostructures have unlocked myriads of functionalities in nanophotonics by engineering light−matter interaction beyond what is possible with conventional bulk optics. The space of parameters available for design is practically unlimited due to the large variety of optical materials and nanofabrication techniques. Thus, computational approaches are necessary to efficiently search for the optimal solutions. In this paper, we enable the free-form inverse design in 3D of linear optical materials with arbitrary dispersion and anisotropy. This is achieved by (1) deriving an analytical adjoint scheme based on the complex-conjugate pole-residue pair model in the time domain and (2) its implementation in a parallel finite-difference time-domain framework with a topology optimization routine, efficiently running on high-performance computing systems. Our method is tested on the design problem of field confinement using dispersive nanostructures. The obtained designs satisfy the fundamental curiosity of how free-form metallic and dielectric nanostructures perform when optimized in 3D, also in comparison to fabrication-constrained designs. Unconventional free-form designs revealed by computational methods, although may be challenging or unfeasible to realize with current technology, bring new insights into how light can more efficiently interact with nanostructures and provide new ideas for forward design.
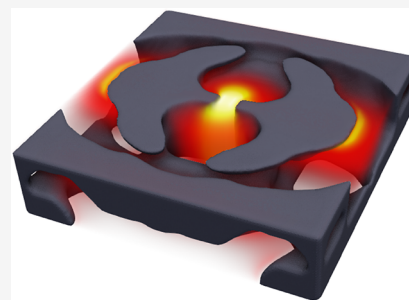
KEYWORDS: adjoint method, FDTD method, topology optimization, optical dispersion, inverse design, time domain

INTRODUCTION

In the past decade, research in nanophotonics has enabled the manipulation and engineering of light−matter interaction at the nanoscale by means of nanostructured materials, such as metasurfaces and metamaterials. This was also made possible by advances in nanofabrication technologies, such as two-photon polymerization, focused ion-beam milling, and lithographic methods, which have enabled the manufacturing of complex structures with features near or below the scale of the electromagnetic wavelength. These combined developments result in compact and efficient optical systems with new functionalities that are difficult or impossible to achieve by using conventional bulk optical components, such as light structuring, beam steering, and dynamic optical control. The design space made available by fabrication techniques and materials is practically unlimited. Exploring large parameter spaces offers opportunities to find innovative designs with improved performance or designs that can satisfy multi-objectives. However, exploring such large parameter spaces is computationally challenging. Numerical methods executed on computers can accelerate the design of optical systems beyond what is achievable via analytical methods and parametric sweeps, which usually start from an initial guess suggested by human intuition. In fact, parameters sweep or stochastic optimization methods, e.g., genetic algorithms, are only suitable to handle problems with few design parameters[1] and therefore only useful when a good initial guess is known. In recent years, inverse design techniques have become popular in (nano-)photonics to automatically and efficiently explore large design spaces and discover and optimize micro- and nanostructures with desired optical functionalities.[2] Deep learning algorithms are emerging as a promising option for nanophotonics inverse design, but they require prohibitively large data sets for training.[3,4] On the contrary, inverse design based on the adjoint method is more efficient since the gradient information used to update the design can be calculated with only two simulations.[5]

Density-based topology optimization (TopOpt) for inverse design originally introduced in mechanical engineering is an iterative design process that allows us to optimize the distribution of a given material in a specified domain in order to optimize a certain objective function.[6−11] This method has been applied to a variety of engineering problems in photonics, such as the optimization of metasurfaces to control certain properties of light (polarization, phase, angular momentum, and achromatic focusing),[12−14] photonic crystals to find optimal omnidirectional band gaps,[15] nanoantennas for

broad-band enhancement,[16] small-scale particle accelerators,[17] quantum emitter and (de-)multiplexers as important components for photonic quantum computers,[18−21] and nonlinear photonic devices for, e.g., second- and third-harmonic generation.[22,23]

Topology optimization via the adjoint method has been presented in various forms based on frequency-domain formulations.[24−26] The treatment of dispersion by frequency-domain solvers, such as the finite element method (FEM) and the finite-difference frequency-domain method is straightforward. The computational complexity of such methods does not increase with the complexity of materials dispersion since only the value of the complex permittivity at the simulation frequency is required. However, a linear system of equations must be solved to obtain the response of a device for each frequency point of interest. As a result, using frequency-domain methods to optimize devices for broadband performance is computationally less efficient since the response at multiple frequencies is required, and there are ongoing efforts to improve frequency-domain solvers in terms of speed and efficiency.[27−29] Hybrid time/frequency domain algorithms have recently been proposed, where the finite-difference time-domain (FDTD) method was used to extract frequency-domain solutions, and the optimization routine itself is performed in the frequency domain.[30,31] For example, the method in reference[30] allows optimization for multiple frequencies using an epigraph formulation.[32,33] This approach also has its trade-offs as the computational cost increases with the number of frequencies for which the optimization algorithm is performed.[30]

The adjoint approach in the time domain is free from this limitation since excitation by temporal signal is designed to contain all the frequencies of interest, which will ultimately result in broadband optimization.[8,16,34] In addition, time-domain methods are in general more versatile for the optimization of time-dependent objectives, such as dynamic phenomena, pulse shaping, and nonstationary transient nonlinear effects. Moreover, time-domain methods scale nearly linearly on high-performance computing systems, thus enabling simulations that can handle optically large domains and/or highly refined mesh.[35] Due to these scalability limitations for large-scale systems, most of the optimizations performed in the frequency-domain focused on problems that can be decomposed by symmetry into 2D problems or 3D designs consisting of planar sheets, with cylindrical symmetry, or with geometric invariance in one direction. In this regard, the optimization of free-form nanostructures in 3D is still an open challenge,[12] and there is a need for algorithms and software implementations to combine flexible inverse design techniques with scalable parallel computing.[30]

In this paper, we tackle two fundamental problems in topology optimization for nanophotonics: (1) the broadband inverse design of arbitrary dispersive materials, including anisotropy, and (2) the inverse design of free-form nanostructures in 3D. For the first point, we introduce a general adjoint scheme based on the time-dependent formulation of Maxwell's equations and the complex-conjugate pole-residue pair (CCPR) model.[36] For the second point, we develop a fully parallel topology optimization algorithm by combining our parallel FDTD solver[35] with a parallel method of moving asymptotes (MMA) open-source routine.[37]

The method is tested, as an example, on the optimization of dispersive nanostructures for field localization. Optical nano-cavities that confine and store light over a broad bandwidth are of great importance to several areas of optics, such as in quantum information for single photon emission,[38,39] spectroscopy,[40,41] coherent plasmon generation,[42] enhancing the interaction between photons and electrons in semiconductor devices (e.g., for lasers),[43] applications in nonlinear optics,[44] or energy harvesting (e.g., in photovoltaics).[45] To date, most nanostructures for field enhancement are invariant in one direction. Although this is typically justified as a fabrication constraint, a move toward 3D free-form optimization is also missing due to the computational challenge associated with such 3D designs. Moreover, the fabrication technology is progressing, for example, via additive manufacturing and two-photon polymerization, and it is timely to satisfy the fundamental curiosity in nanophotonics of what is the shape of optimized free-form nanostructures in 3D. With this question in mind, we demonstrate the universality and efficiency of our method by optimizing free-form 3D metallic and dielectric nanostructures for field confinement under broadband excitation. Investigating the interaction of light with such computer-made complex designs can enable novel functionalities in nanophotonics, as the recently reported anapole in a plasmonic nanostructure.[46] Nanostructures optimized for broadband response in a free-form fashion exhibit shapes and geometries that have never been proposed before, which can later inspire traditional forward design.

■ INVERSE DESIGN OF ARBITRARY DISPERSIVE MATERIALS IN THE TIME DOMAIN

Most materials exhibit dispersion at optical frequencies, which enables various nanophotonic effects in plasmonics, epsilon-near-zero materials, and nonlinear optics. In the literature, various models are used to describe the materials dispersion, such as Debye, Drude, Lorentz, modified Lorentz, and Drude + Critical Points.[36] These models can usually fit one type of material. Although adjoint schemes based on such material models for inverse have been presented in various forms,[16,30] they are limited to only a specific class of materials or tackling only low dispersion problems. This lack of generalizability within the time-domain framework prevents the ability to address different classes of materials within one optimization routine or prevents the optimization of challenging dispersive materials from being considered at all (such as gold in the spectral range of interband transition). The CCPR model was recently proposed as a versatile model that can be used to fit any arbitrary material dispersion, including also the modeling of anisotropy.[36] We employ the CCPR model to inversely design arbitrary dispersive materials aiming at a wide-band performance of nanophotonic devices.

The complex relative permittivity tensor of the CCPR model for an anisotropic, dispersive medium is given by[36]

$$\varepsilon_{\alpha\beta}(\omega) = \varepsilon_{\infty,\alpha\beta} + \frac{\sigma_{\alpha\beta}}{j\omega\varepsilon_0} + \sum_{p=1}^{P_{\alpha\beta}} \left(\frac{c_{p,\alpha\beta}}{j\omega - a_{p,\alpha\beta}} + \frac{c_{p,\alpha\beta}^*}{j\omega - a_{p,\alpha\beta}^*} \right)$$

(1)

where $\varepsilon_{\infty,\alpha\beta}$ is the relative permittivity at infinite frequency, $\sigma_{\alpha\beta}$ is the static electric conductivity, and ε_0 is the vacuum permittivity. We assume the $e^{j\omega t}$ time-dependency. The indices α and β denote the x, y and z component, and * represents the complex conjugation. By a proper selection of its coefficients, the CCPR model can be used to incorporate all the standard dispersive models. Another strength of the model lies in its

ability to accurately fit experimental permittivity data of materials using the vector fitting technique[47,48] or other related algorithms.[49] Figure 1a−d shows the fitting of the experimental
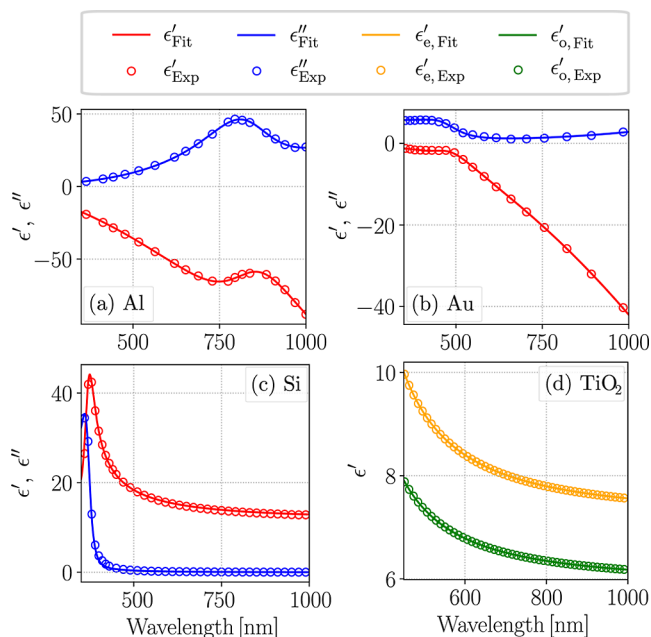

Figure 1. Complex relative permittivity $\varepsilon' - j\varepsilon''$ of (a) Al, (b) Au, (c) Si, and (d) anisotropic TiO$_2$ fitted using the CCPR model in expression (1). We use the experimental data reported in refs 50−53, respectively. The corresponding CCPR parameters are listed in Table 1.

permittivity of aluminum (Al),[50] gold (Au),[51] silicon (Si),[52] and anisotropic titanium dioxide (TiO$_2$),[53] respectively, using the CCPR model. The spectral range of 350−1000 nm corresponds to the range of interest for our broadband optimization. To fit the experimental data, we use three poles for Al and Au, two poles for Si, and a single pole for each axis of the anisotropic TiO$_2$. The ordinary and extraordinary permittivities of titanium dioxide were fitted separately. By choosing the number of CCPR poles, we can compromise between the required fitting accuracy and the computational demand. The coefficients of the fitted model of the four materials are presented in Table 1.

In order to enable density-based topology optimization using the CCPR model, we need an interpolation strategy. In fact, the method requires the description of the material in the design domain as a spatial density distribution ($0 \leq \rho \leq 1$) which is mapped to the material's complex permittivity and consequently describes the topological shape of the photonic

device as the density function converges to a binary design. The interpolation scheme for the CCPR model is presented in the Methods section together with its incorporation into the time-domain Maxwell's equations. We emphasize that our developed topology optimization algorithm can target any arbitrary dispersion of linear materials, and it is required to modify only the model's coefficients and number of poles. In the next section, we describe the optimization setup and the computational challenges associated with it, which results in the adoption of parallel computing in topology optimization.

■ RESULTS AND DISCUSSION

Topology Optimization Setup. In order to handle the topology optimization of arbitrary dispersive materials in time-domain methods, a considerable amount of computational resources is required in terms of memory. This is because the electric field and the auxiliary fields associated with the CCPR model must be stored for all time steps in the entire design domain. The auxiliary fields are needed to model dispersion in the FDTD, and their numbers correspond to the number of CCPR poles used to fit the material permittivity data. For example, storing the fields for the optimization of silicon nanostructures fitted with two CCPR poles, as shown in Figure 1c, results in a three times memory consumption higher than the case of modeling a dispersionless dielectric material.

If we add to this our aim to design 3D free-form nanostructures, then the use of high-performance computing approaches becomes imperative. Therefore, we implemented a fully parallel topology optimization algorithm within our parallel in-house FDTD solver with message passing interface functionalities, whose nearly linear scalability was tested up to 16k cores on a supercomputer.[35] In our parallel software, the simulation region is divided into multiple subregions; each of them updates the fields at every voxel and exchanges the fields on its exterior surfaces with the adjacent subregions.[54] To incorporate topology optimization into our solver, we use the library developed by Aage et al.[55] This library builds on the PETSc ToolKit and provides an efficient implementation of filtering, projecting, and updating of the design using the MMA in parallel.[37]

Here, we describe the optimization problem that leads to the 3D designs presented in the next section. To demonstrate our method, we chose to tackle a canonical problem in nanophotonics: the maximization of the field enhancement in a small volume near a nanostructure. Figure 2 shows the optimization setup. We aim to maximize the electric field energy inside an observation volume Ω_g over a time duration T, by optimizing the topological structure of a given material in the design domain Ω_d that surrounds Ω_g. During the forward simulation, the electric field energy in Ω_g is observed over the

Table 1. CCPR Parameters for the Permittivity Spectral Fitting Are Given in Figure 1

| parameter	Ag	Au	Si	TiO$_2$ (ε_o)	TiO$_2$ (ε_e)
ε_∞	3.07	2.31	1	2.87	3.26
σ	1.49×10^7	1.21×10^7	0	0	0
a_1	-1.89×10^{14}	-1.28×10^{14}	$-8.00 \times 10^{14} + 6.39 \times 10^{15}$j	-6.65×10^{15}j	-6.49×10^{15}j
c_1	-1.00×10^{18}	-6.85×10^{17}	$7.31 \times 10^{14} - 2.89 \times 10^{16}$j	1.01×10^{16}j	1.29×10^{16}j
a_2	$-5.46 \times 10^{14} - 6.37 \times 10^{15}$j	$-6.36 \times 10^{14} - 3.89 \times 10^{15}$j	$-2.32 \times 10^{14} + 5.12 \times 10^{15}$j		
c_2	$1.30 \times 10^{15} + 1.54 \times 10^{15}$j	$2.06 \times 10^{15} + 8.70 \times 10^{14}$j	$4.68 \times 10^{15} - 4.55 \times 10^{15}$j		
a_3	$-5.68 \times 10^{14} - 3.43 \times 10^{14}$j	$-2.96 \times 10^{15} - 6.12 \times 10^{15}$j			
c_3	$1.61 \times 10^{17} + 1.00 \times 10^{12}$j	$1.60 \times 10^{13} + 1.47 \times 10^{16}$j			
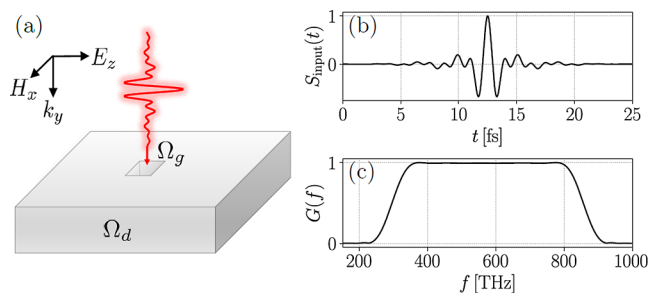
Figure 2. (a) Illustration of the optimization setup. The gap region Ω_g is located at the center of design region Ω_d. We excite the system using a z-polarized plane wave carrying a truncated sinc signal covering the spectral range 350−1000 nm. (b) Time and (c) frequency domain plots of the excitation source.

time duration T until the fields are sufficiently decayed to ensure convergence of the simulation. The objective function, to be maximized, is defined as

$$F[\mathbf{E}] := \frac{\epsilon_0}{2} \int_{\Omega_g} \int_0^T \epsilon_{\infty,g} \mathbf{E}\mathbf{E}\, dt\, d^3r \qquad (2)$$

where we assume that the gap region contains a nondispersive material, air in our case ($\epsilon_{\infty,g} = 1$). We remark that by placing the observation region in eq 2 outside the nanostructure yields other optimization possibilities, such as hybrid nanogap resonators,[38] broadband absorbers (an example is provided in Figure S1 of Supporting Information), or achromatic metalenses.[56] We fix the size of the design problem to $\Omega_d = 100 \times 25 \times 100$ Yee cells for all investigated materials, which can provide a comparison in terms of the required computa-
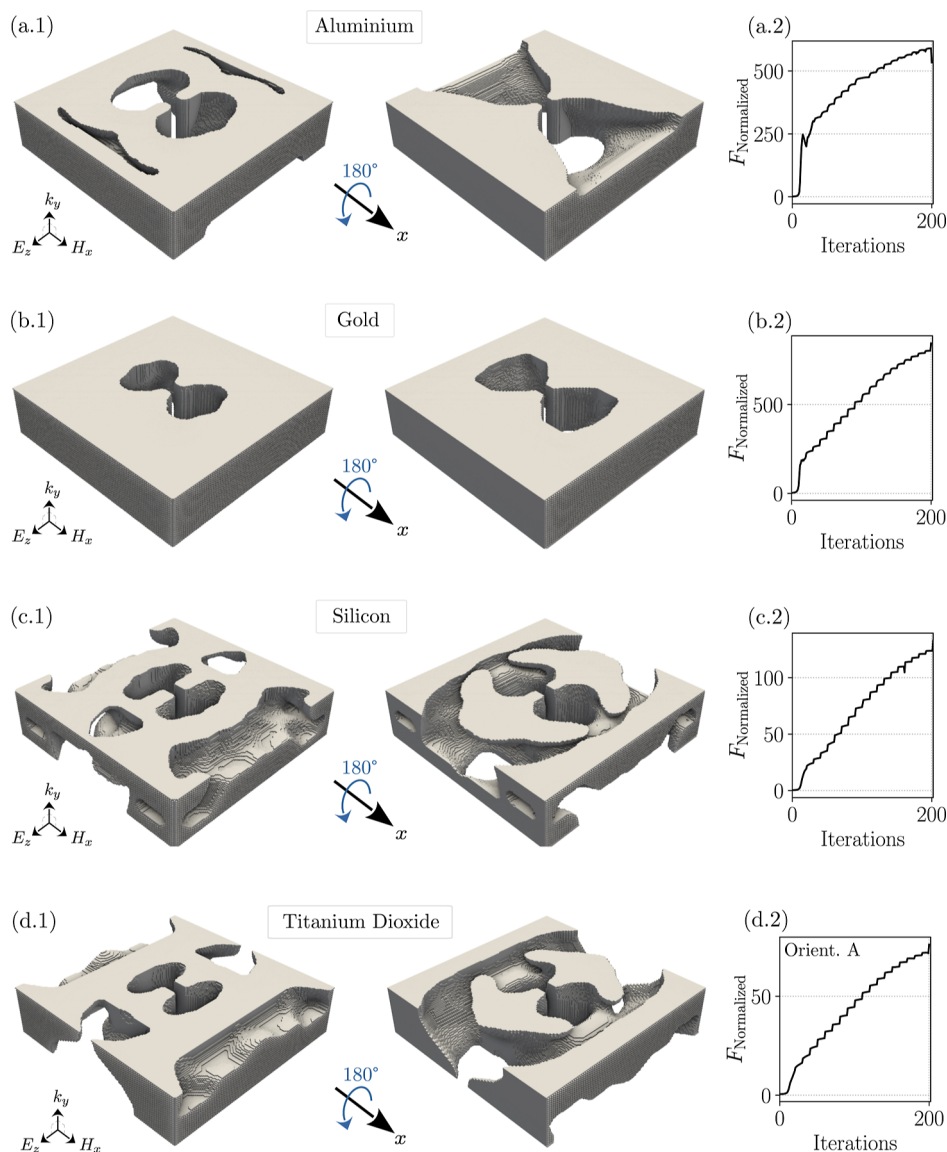

Figure 3. (a.1−d.1) Top and bottom view of the topology-optimized nanostructures for aluminum, gold, silicon, and titanium dioxide. (a.2−d.2) Corresponding progress of relative enhancement inside the gap versus the iteration number during the optimization. The nanostructures are excited by a z-polarized broad band pulse propagating along the positive y-direction. The physical size of the metallic nanostructures is $\Omega_d = 200 \times 50 \times 200$ nm^3 with a gap size of $\Omega_g = 12 \times 50 \times 12$ nm^3. The size of the dielectric nanostructures is $\Omega_d = 500 \times 125 \times 500$ nm^3 with a gap size of $\Omega_g = 30 \times 125 \times 30$ nm^3. For the optimization of the anisotropic titanium dioxide, an alignment of the extraordinary permittivity ϵ_e' axis with the z-axis was considered, while the ordinary permittivity ϵ_o' axis is parallel to the x-axis.
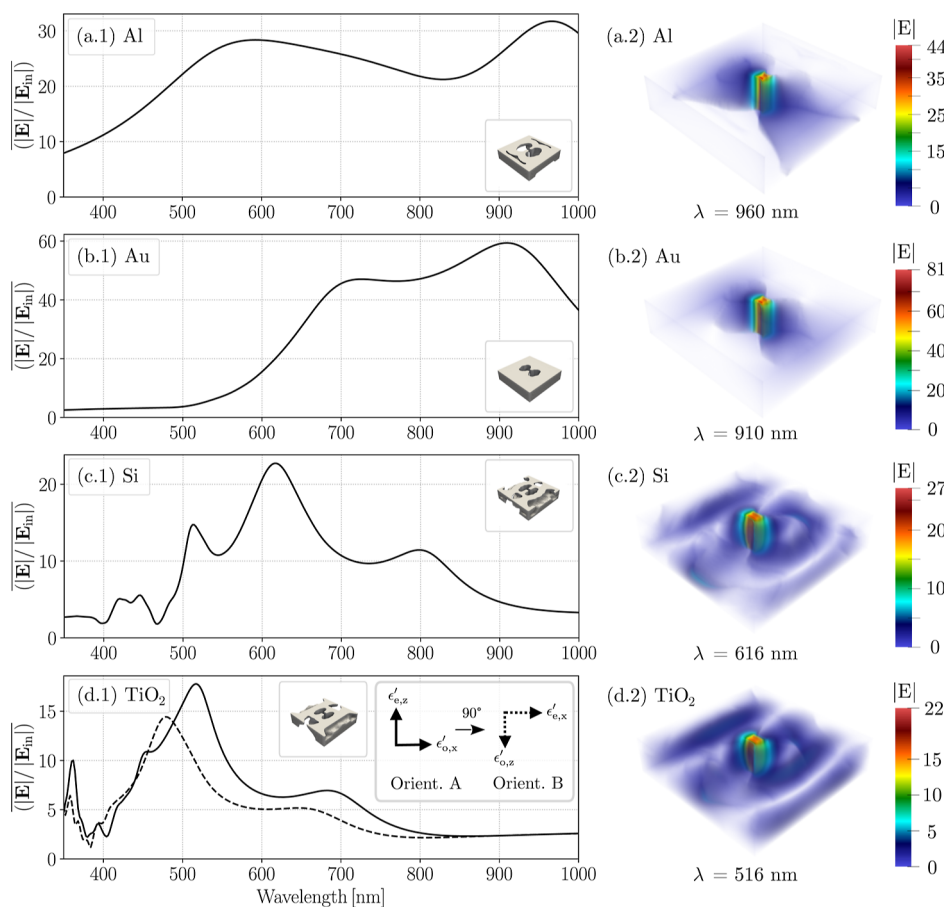
Figure 4. Performance of the nanostructures shown in Figure 3. (a.1−d.1) Average electric field enhancement inside the gap region over the spectral range of excitation. The dashed curve in (d.1) shows the performance of the TiO$_2$ antenna when the original orientation (Orient. A) of the anisotropy is rotated by 90° so that the lower ordinary dielectric constant ϵ_o' is aligned with the polarization of the incident excitation (Orient. B). (a.2−d.2) Corresponding field distribution for the wavelength for which the field enhancement has a maximum.

tional demands. The observation region with a size of $\Omega_g = 6 \times 25 \times 6$ Yee cells is located at the center of Ω_d. We chose a uniform spatial discretization in all directions with space step $\Delta_D = 5$ nm for the optimization of silicon and titanium dioxide and $\Delta_M = 2$ nm for aluminum and gold. This provides a physical domain size that is large enough to capture the different physical effects contributing to the local field enhancement, such as plasmonic and multipole resonances, and ensures enough accuracy for the simulation of all materials using the FDTD method.[35] All parameters used for the optimization as well as the simulation parameters based on the FDTD method are listed in the Methods section.

The excitation signal in Figure 2b is injected as a *z*-polarized plane wave, propagating along the *y* direction. In time-domain topology optimization, the excitation signal defines the target bandwidth. As shown in Figure 2b, the source consists of a sinc signal truncated to a few lobes with a bandwidth of ∼50% at half-maximum. Such a signal modulates a carrier with a frequency of 576.5 THz that corresponds to the center of the spectral window of interest and covers the spectral range 350−1000 nm, as shown in Figure 2c. The excitation signal is also multiplied by a Hanning window to reduce the ripples in the excitation spectrum.

To enable gradient-based topology optimization, we use the adjoint-field method in the time domain to derive a gradient expression for our objective function, defined in expression 2. To compute the gradient of the objective function with respect

to the material density, an additional adjoint simulation must be performed, which differs from the forward simulation only in the source of excitation. Both the forward and adjoint fields observed in the design region Ω_d are then used to compute the spatial gradient profile to update the design at each iteration step. The theoretical and technical details of our method are given in the Methods section and Supporting Information.

In the next section, we demonstrate the flexibility of our inverse design method by aiming at free-form 3D designs enabled by our optimization algorithm for different optical materials with dispersion and anisotropy. We acknowledge that constraints such as length scale or structural invariance along a certain direction can be imposed on the algorithm. Initially, we chose not to impose any of such constraints to explore the free-form optimization. Then, for two study cases, we compare the performance of the free-form designs to structures where invariance along the *y*-direction, as an important lithographic manufacturability constraint, was enforced.

Free-Form 3D Nanostructures. In this section, we present our free-form topology-optimized dispersive metallic (Al and Au) and dielectric (Si and TiO$_2$) nanostructures for broadband field enhancement over the spectral range of 350−1000 nm. The designs obtained based on the optimization setup described in the previous section are illustrated in Figure 3. All optimizations were performed for 200 iterations to ensure a reasonable convergence and to enable a comparison of performance and computational requirements between
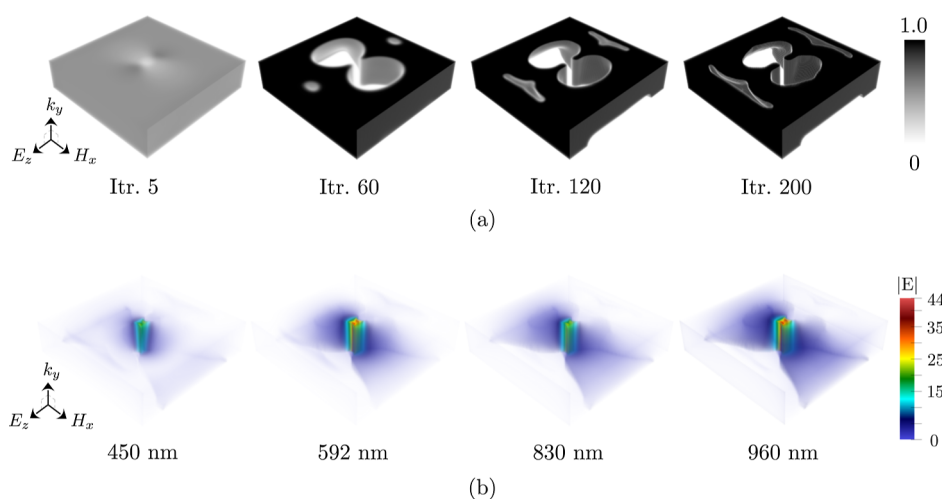
Figure 5. (a) Development of the filtered and projected density $\bar{\bar{\rho}}$ during the optimization of the aluminum nanostructure presented in Figure 3a. The final binary design was obtained by thresholding $\bar{\bar{\rho}}$ at iteration 200 with a projection value of $\eta = 0.5$. (b) Spatial distribution of the electric field magnitude for different wavelengths within the optimized aluminum nanostructure shown in Figure 3a, including the maxima at 592 and 960 nm that appear in the frequency-domain response in Figure 4a.

different materials. We note the difference in shape between top and bottom views for the Al nanostructure in Figure 3a.1, where the left subfigure shows typical features of plasmonic nanostructures,[16] such as a double-hole aperture, while the right subfigure shows features that are typical of metallic antennas in the microwave regime, such as a horn-shape aperture. Also, the Au exhibits typical plasmonic geometrical features, such as a double-hole aperture, that are responsible for field localization and enhancement. This shape was also recently reported to exhibit an anapole state,[46] which is also observed in this case (not shown). The dielectric nanostructures were optimized with a larger space step to allow, at parity of the design domain size, more physical space for the nanostructure to develop. In general, dielectric nanostructures have a larger footprint compared to metallic ones at parity of resonant frequency. In the Si case, we observe the development of complex geometries with a profound difference between top and bottom views, where one side (left) shows an aperture similar to that observed for Au and the other side (right) shows a quasi-free-standing nanostructure. The difference between top and bottom views is remarkable for all materials, and we think this is what enables broadband performance. In the case of Au, although there is a difference in the size of the double-hole aperture in the top and bottom views, the shape of the double-hole does not change significantly, making the overall design very close to a lithographic-constrained structure.

As a measure of the broadband performance, we computed the averaged electric field enhancement inside the gap region over the wavelength range 350−1000 nm, as shown in Figure 4a.1−d.1. In addition, we captured the local field profile for the wavelengths for which the enhancement has a maximum in Figure 4a.2−d.2. The gold and aluminum nanostructures yield a stronger enhancement than the silicon and titanium dioxide nanostructures due to their plasmonic effects and the smaller gap size. From the field distribution plot, we see that the electric field barely penetrates into the bulk in the metallic cases compared with the dielectric designs. The gold nanostructure demonstrates the strongest enhancement, especially for high wavelengths. However, in contrast to aluminum, gold shows a significantly poor performance at low

wavelengths. This can be explained taking the physical properties of gold into account, such as the presence of absorption in this wavelength range associated with the interband transition. In contrast, aluminum is able to enhance the energy at low wavelengths more efficiently. We saw a difference in the topological shape of both materials. The aluminum developed more pronounced carving features compared to gold to maximize the electric energy for the broadband pulse and is apparently bounded by the physical size of the design domain. As a representative example, we plotted the development of the aluminum design during the optimization and the field distributions for multiple wavelengths corresponding to the converged design (Figure 5). Broadband field enhancement is achieved also in the case of the Si nanostructure with several peaks due to the multipole resonances. The field enhancement obtained for Si is lower due to the larger gap size (30 nm vs 12 nm in Au and Al). Although both dielectric designs do not show such a significant difference in the topological shape, we acknowledge a weaker overall performance of titanium dioxide than silicon. Comparing their materials properties in Figure 1c,d, we can attribute it to the fact that the real part of the permittivity of silicon is higher than the ordinary and extraordinary values of titanium dioxide, enabling a more efficient local field enhancement. Also, silicon shows weaker performance for $\lambda < 500$ nm, where it starts being absorptive.

In addition, we studied the performance of the titanium dioxide nanostructure by rotating the anisotropic orientation, on which the antenna was originally designed, by 90°, as shown in Figure 4d.1. The titanium dioxide nanostructure was optimized based on an anisotropic axes orientation, where the extraordinary permittivity ϵ'_e axis is aligned with the z-polarized incident pulse, while the ordinary permittivity ϵ'_o axis is perpendicular to it and oriented along the x-axis. Since $\epsilon'_o < \epsilon'_e$, we obtain a shift of the spectral response to lower wavelengths. This effect is also well-known from Mie resonances and their appearance at certain wavelengths when changing the material's permittivity. The frequency-domain response is highly dependent on the underlying material and dispersion in the desired frequency range as well as the physical size to which the design is constrained. We expect to see deviations in
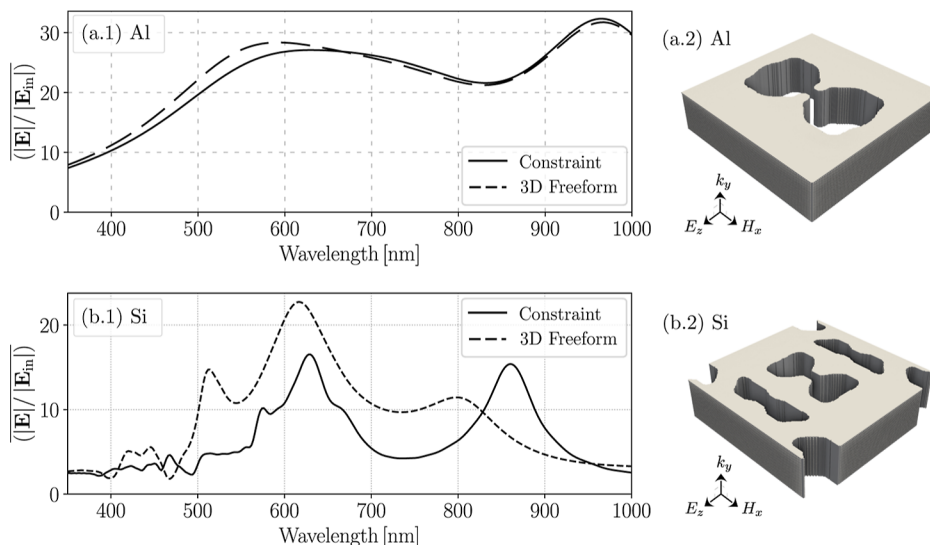
Figure 6. (a.1,b.1) Comparison of the broadband performance of the aluminum and silicon 3D free-form nanostructures shown in Figure 3 with designs where invariance has been constrained along the *y*-direction. (a.2,b.2) Corresponding constraint designs sharing the same physical size as their 3D free-form optimized counterpart.

the frequency-domain response, when modifying the injected source in terms of the spectral content and amplitude.[16] This might enable better control over broadband enhancement, especially by enforcing a better performance in regions of high absorption. One challenging aspect of time-domain optimization is the ability to precisely control the frequency-domain response of the device under test.[9] Attempts to use hybrid approaches to solve such challenging problems emphasize that this issue still requires further investigations.[30]

In addition, we compared our 3D free-form designs to structures where an important lithographic manufacturability constraint was enforced: a fixed thickness (invariance along the *y*-direction), i.e., restricting the design to only vary in the (*x*, *z*)-plane during the optimization process. We chose aluminum and silicon as representatives for metallic and dielectric materials for demonstration purposes. The topology of the optimized structures differs in both cases compared to the free-from-optimized designs, as shown in Figure 6. In the case of aluminum, we notice a slight improvement in the performance of the 3D free-form design compared to its constrained counterpart. More precisely, by allowing the design to expand in the direction of the incoming wave, the structure forms the engraving shown in Figure 3a.1, which results in stronger enhancement for smaller wavelengths. It is obvious that this similarity in the performance is related to the limited physical size. We expect a more significant difference when we give the design more space to expand. The difference in the performance between the free-form and constraint optimizations is significant for the case with silicon. We remark that the physical size here is greater than that for the metallic structures. Interestingly, we see a redistribution of the peaks compared to that of the 3D free form design. Overall, apart from a peak at around 860 nm, the constraint design shows a weaker performance, which highlights the potential of free-from design in 3D for dielectric nanostructures. These results encourage a more detailed investigation of how reducing the degrees of freedom of the design affects the performance (e.g., for large-scale designs).

Contrary to traditional nanostructures for field enhancement, such as dipole and bow-tie nanoantennas, where the two

branches are disconnected and separated via a small gap region, the designs discovered by our algorithm present a similar central gap region but are laterally connected. Although no constraints are given on the connectivity, the volume available for the optimization tends to be filled by the design material, and the final designs look like solid blocks carved with complex topologies. This observation could suggest alternative strategies to design nanostructures with a reduced footprint as well as ideas to improve traditional designs. Free-form optimized nanostructures may also enable exotic physical phenomena, such as anapole meta-atoms.[46] Although such investigations are out of the scope of the current manuscript, in order to promote further studies, we make all of our design and simulation files freely available (see data availability statement).

■ METHODS

Time-Domain Adjoint Formulation. In this section, we formulate the density-based topology optimization problem for dispersive materials in time-domain. We use the adjoint method to derive the gradient expression for an objective $F[\mathbf{E}]$, where $\mathbf{E}$ is the electric field that depends on a density distribution ρ that represents our design variables. The objective function and its gradient are needed for gradient-based optimization algorithms. The full derivation is given in the Supporting Information.

We formulate the conceptual optimization problem

$$\max_{\rho(\mathbf{r})} F \quad [\mathbf{E}(\mathbf{r}, t)]$$

$$\text{s. t.} \quad \text{Maxwell's equations} \tag{3}$$

We assume nonmagnetic materials. All of the following derivations, however, can also be conducted for the magnetic permeability tensor and magnetic field $\mathbf{H}(\mathbf{r}, t)$. The density is mapped to the physical material described by the CCPR model in expression 1. In the following, we denote the background material with index i = 1 and the design material with index i = 2. For a given density value $\rho \in [0, 1]$, we apply a linear interpolation of the parameters and complex pole pairs in expression 1 of the following form
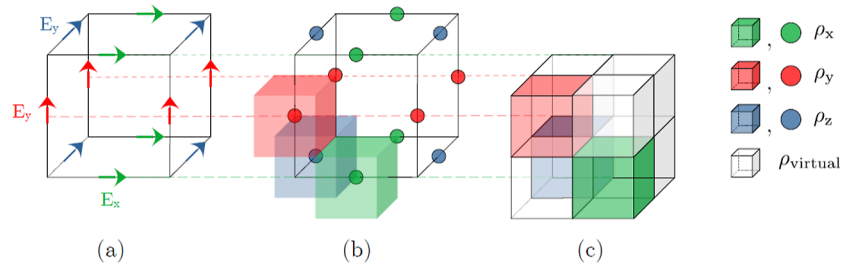
Figure 7. (a) According to the FDTD method, the electric field components are stored on a staggered grid. Each component E_k is placed at the center of the corresponding edge of the Yee cell. (b) Definition of subcells, being half as wide and locally offset by a quarter of the width of the Yee cell in each direction. Each of these cells encapsulates a density point ρ_k to the associated electric field component. (c) Empty space is filled with virtual subcells, encapsulating undefined density values ρ_{virtual}. Their values must be assigned by a proper filtering, taking the defined values of neighboring subcells into account.

$$\varepsilon_{\infty,\alpha\beta}(\rho) := (1 - \rho)\varepsilon_{\infty,\alpha\beta}^{(1)} + \rho\varepsilon_{\infty,\alpha\beta}^{(2)} \qquad (4)$$

$$\sigma_{\alpha\beta}(\rho) := (1 - \rho)\sigma_{\alpha\beta}^{(1)} + \rho\sigma_{\alpha\beta}^{(2)} + \rho(1 - \rho)\gamma \qquad (5)$$

$$\Sigma_{\alpha\beta}(\omega, \rho) := \sum_{i=1}^{2} \sum_{p=1}^{P_{\alpha\beta}^{(i)}} \kappa^{(i)}(\rho)\left(\frac{c_{p,\alpha\beta}^{(i)}}{j\omega - a_{p,\alpha\beta}^{(i)}} + \frac{c_{p,\alpha\beta}^{(i)*}}{j\omega - a_{p,\alpha\beta}^{(i)*}} \right) \qquad (6)$$

where $\kappa^{(1)}(\rho) := (1 - \rho)$ and $\kappa^{(2)}(\rho) := \rho$. For the static conductivity in expression 5, we added an additional damping term γ, which can be tuned to avoid zero crossings of the permittivity (e.g., for metals) for intermediate values of ρ, inhibiting the optimization convergence.[16,30] The interpolated relative permittivity can be written as

$$\varepsilon_{\alpha\beta}(\omega, \rho) = \varepsilon_{\infty,\alpha\beta}(\rho) + \sigma_{\alpha\beta}(\rho) + \Sigma_{\alpha\beta}(\omega, \rho) \qquad (7)$$

For simplicity, we assume the permittivity of both design and background material to be diagonal, $\varepsilon_{\alpha\beta} = 0$ for $\alpha \neq \beta$, and denote the spatial component of permittivity and fields by $k \in \{x, y, z\}$.

For the formulation of the adjoint problem to maximize an objective $F[\mathbf{E}]$, we follow a similar approach as in ref 16 with the same boundary conditions, but replacing the material model by our CCPR model. The electric field components E_k, $k \in \{x, y, z\}$, of the forward system driven by an incident pulse injected far away from the design and observation region can be obtained by solving the Maxwell equations

$$(\nabla \times \mathbf{H})_k + \varepsilon_0\varepsilon_{\infty,k}(\rho)\partial_t E_k + \sigma(\rho)_k E_k + 2\sum_{i=1}^{2} \kappa^{(i)}(\rho)\Re\left\{ \sum_{p=1}^{P_k^{(i)}} \partial_t Q_{p,k}^{(i)} \right\} = 0 \qquad (8a)$$

$$\text{For } i = 1, 2 \text{ and } \forall\, p \in 1, ..., P_k^{(i)}: \partial_t Q_{p,k}^{(i)} - a_{p,k}^{(i)} Q_{p,k}^{(i)} - c_{p,k}^{(i)} E_k = 0 \qquad (8b)$$

$$\mu_0\partial_t H_k + (\nabla \times \mathbf{E})_k = 0 \qquad (8c)$$

where the complex auxiliary fields $Q_{p,k}^{(i)}$ must be computed for all poles $p \in 1,..., P_k^{(i)}$ and for the corresponding component k of both materials i = 1, 2. To compute the gradient of the objective with respect to the density, an additional adjoint system must be solved, which differs from the forward system only in the source of excitation. The adjoint fields $\tilde{E}_k$, $\tilde{H}$, and $\tilde{Q}_{p,k}^{(i)}$ are obtained by solving the same set of equations but introducing a source term $\mathbf{S}_{\text{adj}}$ on the right-hand side of eq 8a, which acts as the source for the adjoint system instead of the plane wave injected into the forward system. The adjoint source is the time-reversed (denoted by the symbol "←") functional derivative of the objective $F[\mathbf{E}]$ with respect to the forward field: $\mathbf{S}_{\text{adj}} := \overleftarrow{\frac{\delta F[\mathbf{E}]}{\delta \mathbf{E}}}$. The expression for the adjoint system as well as for the gradient can be obtained as follows (see the Supporting Information). First, we differentiate eqs (8) with respect to the density, and multiply eq 8a by $\tilde{E}_k$, eq 8c by $\tilde{H}_k$, and each of eq 8b by a corresponding term $-\frac{\kappa^{(i)}(\rho)}{\varepsilon_0 c_{p,k}^{(i)}}\partial_t\tilde{Q}_{p,k}^{(i)}$, assuming a nonvanishing parameters $c_{p,k}^{(i)} \neq 0$. We further sum all spatial components and integrate over time

and space, taking the imposed boundary conditions of the forward fields into account. Then, we reverse the time $t \to \tau := T - t$ and change the signs of the adjoint magnetic fields and currents,[57] which leads to the adjoint system as described before. Moreover, we obtain the expression for the gradient of the objective function with respect to the density

$$\nabla_\rho F := -\int_0^T \sum_{k=1}^{3} \varepsilon_0\partial_\rho\varepsilon_{\infty,k}(\rho)\overleftarrow{E}_k\partial_t\tilde{E}_k \, dt$$

$$-\int_0^T \sum_{k=1}^{3} \partial_\rho\sigma_k(\rho)\overleftarrow{E}_k\tilde{E}_k \, dt$$

$$+\int_0^T \sum_{k=1}^{3} \sum_{i=1}^{2} \sum_{p=1}^{P_k^{(i)}} 2\partial_\rho\kappa^{(i)}(\rho)\Re\{\partial_t\overleftarrow{Q}_{p,k}^{(i)}\}\tilde{E}_k \, dt$$

$$(9)$$

The derived expression also covers nondispersive dielectric materials by simply setting all coefficients to 0, except for the $\varepsilon_{\infty,k}$ terms, leaving only the first term in expression 9.

FDTD Implementation and Design Export. According to the FDTD method, each component of the electric and
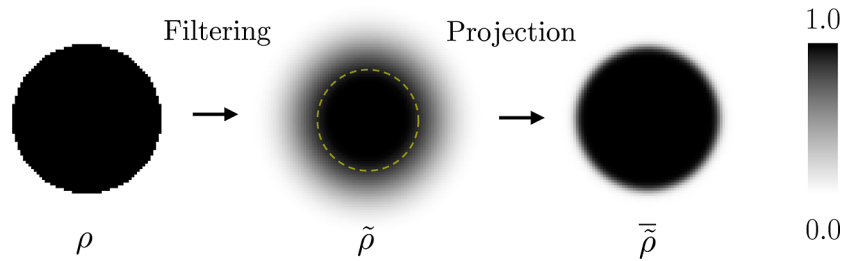
Figure 8. Demonstration of the filtering and projection of the density in 2D. The original density ρ representing a sphere with a radius R_0 is filtered according to eq 12 with a filter radius of $R = 0.3R_0$, marked as a yellow dashed circle. The filtered density $\tilde{\rho}$ will be projected using the smoothed Heaviside function in eq 14 to obtain $\bar{\tilde{\rho}}$, which is used as an input for the forward and adjoint simulation. Here, projection parameters $\beta = 10$ and $\eta = 0.5$ were used.

magnetic field is placed at different locations of the Yee cell (Figure 7a).[58] If the design region is divided into $N := N_x \times N_y \times N_z$ Yee cells, we assign density values $\rho_{k,n}, n \in \{1, ..., \tilde{N}_k\}$ at each location of the electric field components E_k, where $\tilde{N}_k$ is defined as

$$\tilde{N}_k := \prod_{l \in \{x,y,z\}} (N_l + 1 - \delta_{kl}) \tag{10}$$

with δ_{kl} denoting the Kronecker delta. Here, the additional $1 - \delta_{kl}$ cells ensure an accurate description of the design domain boundaries. As a consequence, we optimize $\tilde{N} := \sum_{k \in \{x,y,z\}} \tilde{N}_k$ design variables in total.

The update equations for the fields in eqs (8) within the FDTD framework are discussed in detail in ref 36. The gradient of the objective function in expression 9 with respect to each design variable $\rho_{k,n}$ can be discretized in a similar manner[57]

$$\nabla_{\rho_{k,n}} F := - \varepsilon_0 (\varepsilon_{\infty,k,n}^{(2)} - \varepsilon_{\infty,k,n}^{(1)}) \sum_{m=1}^{M} E_{k,n}^{M-m} (\tilde{E}_{k,n}^{m+1/2} - \tilde{E}_{k,n}^{m-1/2})$$

$$- (\sigma_{k,n}^{(2)} - \sigma_{k,n}^{(1)} + (1 - 2\rho_{k,n})\gamma) \sum_{m=1}^{M} E_{k,n}^{M-m} \frac{\tilde{E}_{k,n}^{m+1/2} + \tilde{E}_{k,n}^{m-1/2}}{2} \Delta t$$

$$+ 2 \sum_{m=1}^{M} \sum_{i=1}^{2} \sum_{p=1}^{P_k^{(i)}} \partial_\rho \kappa^{(i)} \Re\{Q_{p,k,n}^{M-m,(i)} - Q_{p,k,n}^{M-(m-1),(i)}\} \frac{\tilde{E}_{k,n}^{m+1/2} + \tilde{E}_{k,n}^{m-1/2}}{2} \tag{11}$$

where $\partial_\rho \kappa^{(1)} = -1$ and $\partial_\rho \kappa^{(2)} = 1$, Δt denotes the time discretization, and M is the maximum number of time steps that corresponds to the simulation time.

When the optimization is complete and all density values are binarized after a proper thresholding, the design must be saved so that it is transferable to other software for simulation or to a software for planning the manufacturing, e.g., as STL file. To do so, we need to define a smallest volume (*Wigner-Seitz cell*) around each density point so that their adjacent arrangement would fill the entire space without leaving any gaps or holes.

In this way, material or no material can be assigned to each cell to build and visualize the final design. Due to the lack of symmetry of the staggered Yee grid in 3D, the construction of such a cell is not possible. Therefore, we construct a symmetric material grid by dividing each Yee cell into eight subcells, which are half as wide and locally offset by a quarter of the width of the original cell in each direction (Figure 7b,c). In that way, each density point located at the edges of the Yee cell is encapsulated by a subcell. For the other five undefined, virtual subcells, we perform an interpolation, by averaging over the next neighbors, including the noninterpolated density points only. This interpolation scheme leaves the assignment of the original density points at the edges untouched and well-defined and is, therefore, transferable to any FDTD framework, assigning the material for the staggered grid in reverse.

Filtering and Projection. Filtering is an effective way of introducing a weak sense of length scale into the design, to eradicate the appearance of single-pixel features[59,60] or to cure the self-penalization issue when optimizing lossy structures.[9,61,62] To control spatial design-field variations, we filter the design variables and apply a threshold procedure. Assuming we have $\tilde{N}$ design variables in total, we enumerate the variables with the index $n \in \{1, ..., \tilde{N}\}$ in the following. At each iteration step and for each density point ρ_n, we average over a neighborhood set of densities to obtain the filtered variable $\tilde{\rho}_n$

$$\tilde{\rho}_n = \frac{\sum_{\rho_m \in \mathcal{B}_R^n} w(\mathbf{r}_n, \mathbf{r}_m)\rho_m}{\sum_{\rho_m \in \mathcal{B}_R^n} w(\mathbf{r}_n, \mathbf{r}_m)} \tag{12}$$

where $\mathcal{B}_R^n$ describes a sphere with radius R around ρ_n. $w(\mathbf{r}_n, \mathbf{r}_m)$ is the weighting function defined as

$$w(\mathbf{r}_n, \mathbf{r}_m) = R - |\mathbf{r}_m - \mathbf{r}_n| \tag{13}$$

and ensures that values at a greater distance contribute less. Next, we project the filtered density using the smoothed Heaviside function

$$\bar{\tilde{\rho}}_n = \frac{\tanh(\beta\eta) + \tanh(\beta(\tilde{\rho}_n - \eta))}{\tanh(\beta\eta) + \tanh(\beta(1 - \eta))} \tag{14}$$

The parameter η determines the threshold value, and β controls the sharpness of the projection, consequently leading to the binary design for $\beta \rightarrow \infty$. Figure 8 demonstrates the filtering and projecting procedure for a spherical density in 2D.

The gradient of the objective with respect to the original density ρ can be calculated using the chain rule

$$\frac{\partial F}{\partial \rho_n} = \sum_{\rho_m \in \mathcal{B}_R^n} \frac{\partial F}{\partial \bar{\bar{\rho}}_m} \frac{\partial \bar{\bar{\rho}}_m}{\partial \tilde{\rho}_m} \frac{\partial \tilde{\rho}_m}{\partial \rho_n} \tag{15}$$

The β value will be increased during the optimization until the objective does not show any significant change, yielding an almost binary design. One way to tell whether an optimized design has converged to a discrete solution is to use the measure of discreteness[63]

$$M_{nd} = \frac{\sum_{n=1}^{\tilde{N}} 4\bar{\bar{\rho}}_n (1 - \bar{\bar{\rho}}_n)}{\tilde{N}} \times 100\% \tag{16}$$

This measure is zero if the design only consists of elements with a 0 or 1 density and gets maximized if all density points have an intermediate value of 0.5. Finally, the projected density is mapped to a binary design by thresholding with respect to the parameter η. The final design in the FDTD framework is exported by the interpolation scheme described in the previous section.

Technical Details of the Optimization. In this section, we list the parameters used for the topology optimization of the nanostructures presented in the paper. It includes the simulation parameters for the FDTD method that were used to perform the forward and adjoint simulation as well as the filter and projection variables to transform the density at each iteration step and technical details about how the simulations were performed, including the parallelization strategy.

The design region Ω_d consists of $100 \times 25 \times 100$ Yee cells. The observation region with $6 \times 25 \times 6$ cells is located at the center of Ω_d (see Figure 2a). The design region is surrounded by convolutional perfectly matched layer layers with a thickness of 20 Yee cells. We chose an isotropic spatial discretization $\Delta := dx = dy = dz$ and set its value small enough to ensure a sufficient accuracy while performing the FDTD simulations for all chosen materials.[35] We set $\Delta_D = 5$ nm for the optimization of silicon and titanium dioxide, and $\Delta_M = 2$ nm for aluminum and gold. We aim to optimize a $\Omega_d = 200 \times 50 \times 200$ nm^3 aluminum and gold nanostructure with a gap size of $\Omega_g = 12 \times 50 \times 12$ nm^3, and for a $\Omega_d = 500 \times 125 \times 500$ nm^3 silicon and titanium dioxide nanostructure with a gap size of $\Omega_g = 30 \times 125 \times 30$ nm^3. We chose a time discretization of $dt = 8.34 \times 10^{-3}$ fs for both dielectrics and performed forward and adjoint simulations for 10,000 time steps, which corresponds to a time duration $T = 83.40$ fs in eq 2. For metals, we chose $dt = 3.34 \times 10^{-3}$ fs and 18,000 time steps, corresponding to $T = 60.12$ fs. This parameter setting ensured Courant stability and a sufficient decay of the fields so that the objective and gradient did not show a significant change at the end of each forward or adjoint simulation.

For all materials, an artificial damping $\gamma = 500,000$ was chosen in eq 5, to ensure convergence. The proper choice of this parameter is discussed in ref 16. For the radius of the filter, we chose $R = 12$ Yee cells, corresponding to a radius of $R_D = 60$ nm for dielectrics and $R_M = 24$ nm for metals. Starting with an initial projection value of $\beta_0 = 10^{-4}$, we run each optimization for 200 iterations, increasing β up to a value of

$\beta_{\max} = 52$. The threshold value was set to $\eta = 0.5$. The maximum number of iteration together with $\beta_{\max}$ ensured that the density $\bar{\bar{\rho}}$ does not contain larger gray areas of intermediate density values between 0 and 1 before thresholding, i.e., performing a binarization of $\bar{\bar{\rho}}$. For verification, we computed the measure of discreteness of the final designs according to eq 16 and obtained: $M_{nd}^{Al} = 1.0229\%$, $M_{nd}^{Au} = 0.3918\%$, $M_{nd}^{Si} = 1.8153\%$, and $M_{nd}^{TiO_2} = 1.1907\%$. The densities were updated by the MMA.[64]

The optimizations were performed with our in-house FDTD code, and we used the commercial software *Ansys Lumerical* to cross verify the performance of the final optimized designs. The simulations were performed on the supercomputer *HLRN-IV-System Emmy* in Göttingen, Germany, provided by the *North German Supercomputing Alliance* as part of the National High Performance Computing (NHR) infrastructure. It took ≈2−14 h to optimize the structures presented in this paper, using 1536 cores (Cascade 9242, HLRN-IV-System Emmy in Göttingen, Germany). The computation time depends on the number of the CCPR poles used in the simulation. Since the part of the simulation domain containing the design region needs to perform additional tasks and requires additional memory due to the storage of the electric and auxiliary field, a parallelization strategy based on a uniform decomposition of the simulation domain among the processors would not be efficient. Thus, we applied a load-balancing scheme in which the density domain ($100 \times 25 \times 100 = 250,000$ Yee cells) was assigned to 576 cores, and the remaining simulation domain ($150 \times 78 \times 150 - 250,000 = 1,505,000$ Yee cells) was divided among the remaining 960 cores. This refinement ensured an improved speedup and memory allocation.

CONCLUSIONS

We introduced a general density-based topology optimization approach to the inverse design of arbitrary dispersive and anisotropic nanophotonic structures. The optimization problem is formulated in the time domain based on the CCPR model. We employ the auxiliary equations approach to Maxwell's equations and derive an adjoint system that allows us to compute the gradient using only two system solutions. By choice of the number of CCPR poles, a compromise between the required fitting accuracy and the computational requirements can be found. The formulation of the figure of merit and corresponding adjoint source is kept in a general form and is interchangeable so that the method can be applied on various design problems in optics.

The method was implemented in our highly parallelized FDTD code, and we provided an interpolation scheme to extract the final design from the staggered Yee grid. The reliability of the method is demonstrated by designing dielectric and metallic nanostructures for local broadband enhancement, enabling free-form optimization in 3D. By combining parallel topology optimization and parallel FDTD solver, we unlock not only the design of arbitrary dispersive materials but also the free-form optimization of nanostructures. We note that the presented adjoint method is not limited to the FDTD method but is given in analytical form and thus could be implemented in a time-domain FEM framework with an auxiliary field approach included.[65]

Despite the computational effort required for free-form optimization in 3D and the limitations of current manufactur-

ing techniques, our results give insights into which topological features may lead to an enhancement of light−matter interactions at the nanoscale, thus expanding the set of shapes used in traditional design. Beside the presented optimization of nanocavities of different material classes, our contribution holds great potential for a variety of other inverse design problems where dispersion is included, such as broadband absorbers using plasmonic metals, highly absorbing nanostructured thin-films for maximizing the efficiency of solar cells, or broadband antireflective coating based on dielectrics. Moreover, our adjoint time-domain formulation allows us to tackle any design problem where time-dependent objectives are appropriate, such as dynamic phenomena, transient nonlinear effects, or considering time-varying materials. Due to the increasing interest in time-domain phenomena in nanophotonics and relative methodologies, this method is likely to become very relevant in the near-future for the solution of many interesting inverse design problems.

◼ ASSOCIATED CONTENT

Data Availability Statement

All design files (in the STL format) and Ansys Lumerical files used for the simulations presented in the paper are openly available at the following URL/DOI: 10.5281/zeno-do.7820727.

ⓈⒾ Supporting Information

The Supporting Information is available free of charge at https://pubs.acs.org/doi/10.1021/acsphotonics.3c00572.

> Full derivation of the gradients as well as a demonstration of the inverse design of a broadband absorber (PDF)

◼ AUTHOR INFORMATION

Corresponding Authors

Johannes Gedeon − *Hannover Centre for Optical Technologies, Institute for Transport and Automation Technology (Faculty of Mechanical Engineering), and Cluster of Excellence PhoenixD, Leibniz University Hannover, 30167 Hannover, Germany;* ⓞ orcid.org/0000-0002-5060-7535; Email: johannes.gedeon@hot.uni-hannover.de

Emadeldeen Hassan − *Department of Electronics and Electrical Communications, Menoufia University, Menouf 32952, Egypt; Department of Applied Physics and Electronics, Umeå University, SE-901 87 Umeå, Sweden;* ⓞ orcid.org/0000-0002-1318-7519; Email: emadeldeen.hassan@umu.se

Antonio Calà Lesina − *Hannover Centre for Optical Technologies, Institute for Transport and Automation Technology (Faculty of Mechanical Engineering), and Cluster of Excellence PhoenixD, Leibniz University Hannover, 30167 Hannover, Germany;* ⓞ orcid.org/0000-0002-9384-6245; Email: antonio.calalesina@hot.uni-hannover.de

Complete contact information is available at:
https://pubs.acs.org/10.1021/acsphotonics.3c00572

Notes

The authors declare no competing financial interest.
A preprint version of this article is available online (https://arxiv.org/abs/2305.00234).

◼ ACKNOWLEDGMENTS

◼ REFERENCES

(1) Sigmund, O. On the usefulness of non-gradient approaches in topology optimization. *Struct. Multidiscipl. Optim.* **2011**, *43*, 589−596.

(2) Molesky, S.; Lin, Z.; Piggott, A. Y.; Jin, W.; Vucković, J.; Rodriguez, A. W. Inverse design in nanophotonics. *Nat. Photonics* **2018**, *12*, 659−670.

(3) Jiang, J.; Chen, M.; Fan, J. A. Deep neural networks for the evaluation and design of photonic devices. *Nat. Rev. Mater.* **2020**, *6*, 679−700.

(4) Ma, W.; Liu, Z.; Kudyshev, Z. A.; Boltasseva, A.; Cai, W.; Liu, Y. Deep learning for the design of photonic structures. *Nat. Photonics* **2021**, *15*, 77−90.

(5) Deng, Y. *Adjoint Topology Optimization Theory for Nano-Optics*; Springer, 2022.

(6) Bendsøe, M. P.; Sigmund, O. *Topology Optimization*; Springer: Berlin Heidelberg, 2004.

(7) Jensen, J. S.; Sigmund, O. Topology optimization for nanophotonics. *Laser Photonics Rev.* **2011**, *5*, 308−321.

(8) Nomura, T.; Sato, K.; Taguchi, K.; Kashiwa, T.; Nishiwaki, S. Structural topology optimization for the design of broadband dielectric resonator antennas using the finite difference time domain technique. *Int. J. Num. Meth. Eng.* **2007**, *71*, 1261−1296.

(9) Hassan, E.; Wadbro, E.; Berggren, M. Topology Optimization of Metallic Antennas. *IEEE Trans. Antennas Propag.* **2014**, *62*, 2488−2500.

(10) Elesin, Y.; Lazarov, B. S.; Jensen, J. S.; Sigmund, O. Time domain topology optimization of 3D nanophotonic devices. *Photonics Nanostructures-Fundam. Appl.* **2014**, *12*, 23−33.

(11) Hassan, E.; Scheiner, B.; Michler, F.; Berggren, M.; Wadbro, E.; Rohrl, F.; Zorn, S.; Weigel, R.; Lurz, F. Multilayer Topology Optimization of Wideband SIW-to-Waveguide Transitions. *IEEE Trans. Microw. Theory Technol.* **2020**, *68*, 1326−1339.

(12) Li, Z.; Pestourie, R.; Lin, Z.; Johnson, S. G.; Capasso, F. Empowering Metasurfaces with Inverse Design: Principles and Applications. *ACS Photonics* **2022**, *9*, 2178−2192.

(13) White, A. D.; Su, L.; Shahar, D. I.; Yang, K. Y.; Ahn, G. H.; Skarda, J. L.; Ramachandran, S.; Vučković, J. Inverse Design of Optical Vortex Beam Emitters. *ACS Photonics* **2022**, *10*, 803−807.

(14) Yasuda, H.; Nishiwaki, S. A design method of broadband metalens using time-domain topology optimization. *AIP Adv.* **2021**, *11*, 055116.

(15) Men, H.; Lee, K. Y. K.; Freund, R. M.; Peraire, J.; Johnson, S. G. Robust topology optimization of three-dimensional photonic-crystal band-gap structures. *Opt. Express* **2014**, *22*, 22632−22648.

(16) Hassan, E.; Calà Lesina, A. Topology optimization of dispersive plasmonic nanostructures in the time-domain. *Opt. Express* **2022**, *30*, 19557−19572.

(17) Sapra, N. V.; Yang, K. Y.; Vercruysse, D.; Leedle, K. J.; Black, D. S.; England, R. J.; Su, L.; Trivedi, R.; Miao, Y.; Solgaard, O.; Byer, R.

L.; Vučković, J. On-chip integrated laser-driven particle accelerator. *Science* **2020**, *367*, 79–83.

(18) Yesilyurt, O.; Kudyshev, Z. A.; Boltasseva, A.; Shalaev, V. M.; Kildishev, A. V. Efficient Topology-Optimized Couplers for On-Chip Single-Photon Sources. *ACS Photonics* **2021**, *8*, 3061–3068.

(19) Frandsen, L. H.; Sigmund, O. Inverse design engineering of all-silicon polarization beam splitters. *SPIE Proc.* **2016**, *9756*, 97560Y.

(20) Piggott, A. Y.; Lu, J.; Lagoudakis, K. G.; Petykiewicz, J.; Babinec, T. M.; Vuckovic, J. Inverse design of a wavelength demultiplexer. In *2016 Conference on Lasers and Electro-Optics (CLEO)*, 2016; pp 1−2.

(21) Frellsen, L. F.; Ding, Y.; Sigmund, O.; Frandsen, L. H. Topology optimized mode multiplexing in silicon-on-insulator photonic wire waveguides. *Opt. Express* **2016**, *24*, 16866−16873.

(22) Lin, Z.; Liang, X.; Loncar, M.; Johnson, S.; Rodríguez, A. Cavity-enhanced second harmonic generation via topology optimization. In *Frontiers in Optics*, 2015; p FM1D.3.

(23) Hughes, T. W.; Minkov, M.; Williamson, I. A. D.; Fan, S. Adjoint Method and Inverse Design for Nonlinear Nanophotonic Devices. *ACS Photonics* **2018**, *5*, 4781−4787.

(24) Deng, Y. *Adjoint Topology Optimization Theory for Nano-Optics*, 1st ed.; Springer Nature Singapore, 2022.

(25) Christiansen, R. E.; Vester-Petersen, J.; Madsen, S. P.; Sigmund, O. A non-linear material interpolation for design of metallic nano-particles using topology optimization. *Comput. Methods Appl. Mech. Eng.* **2019**, *343*, 23−39.

(26) Wadbro, E.; Engström, C. Topology and shape optimization of plasmonic nano-antennas. *Comput. Methods Appl. Mech. Eng.* **2015**, *293*, 155−169.

(27) Zhao, N.; Verweij, S.; Shin, W.; Fan, S. Accelerating convergence of an iterative solution of finite difference frequency domain problems via schur complement domain decomposition. *Opt. Express* **2018**, *26*, 16925−16939.

(28) Lin, H.-C.; Wang, Z.; Hsu, C. W. Fast multi-source nanophotonic simulations using augmented partial factorization. *Nat. Comput. Sci.* **2022**, *2*, 815−822.

(29) Zhao, N. Z. *Accelerating Numerical Methods for Gradient-Based Photonic Optimization and Novel Plasmonic Functionalities*; Stanford University, 2004.

(30) Hammond, A. M.; Oskooi, A.; Chen, M.; Lin, Z.; Johnson, S. G.; Ralph, S. E. High-performance hybrid time/frequency-domain topology optimization for large-scale photonics inverse design. *Opt. Express* **2022**, *30*, 4467−4491.

(31) Zeng, Z.; Venuthurumilli, P. K.; Xu, X. Inverse Design of Plasmonic Structures with FDTD. *ACS Photonics* **2021**, *8*, 1489−1496.

(32) Boyd, S.; Vandenberghe, L. *Convex Optimization*; Cambridge University, 2004.

(33) Svanberg, K. A. A Class of Globally Convergent Optimization Methods Based on Conservative Convex Separable Approximations. *SIAM J. Optim.* **2002**, *12*, 555−573.

(34) Hassan, E.; Wadbro, E.; Hägg, L.; Berggren, M. Topology optimization of compact wideband coaxial-to-waveguide transitions with minimum-size control. *Struct. Multidiscip. Optim.* **2018**, *57*, 1765−1777.

(35) Calà Lesina, A.; Vaccari, A.; Berini, P.; Ramunno, L. On the convergence and accuracy of the FDTD method for nanoplasmonics. *Opt. Express* **2015**, *23*, 10481−10497.

(36) Prokopidis, K. P.; Zografopoulos, D. C. Time-Domain Studies of General Dispersive Anisotropic Media by the Complex-Conjugate Pole−Residue Pairs Model. *Appl. Sci.* **2021**, *11*, 3844.

(37) Aage, N.; Lazarov, B. S. Parallel Framework for Topology Optimization Using the Method of Moving Asymptotes. *Struct Multidiscip Optim.* **2013**, *47*, 493−505.

(38) Sugimoto, H.; Fujii, M. Broadband Dielectric−Metal Hybrid Nanoantenna: Silicon Nanoparticle on a Mirror. *ACS Photonics* **2018**, *5*, 1986−1993.

(39) Maksymov, I. S.; Besbes, M.; Hugonin, J. P.; Yang, J.; Beveratos, A.; Sagnes, I.; Robert-Philip, I.; Lalanne, P. Metal-Coated

Nanocylinder Cavity for Broadband Nonclassical Light Emission. *Phys. Rev. Lett.* **2010**, *105*, 180502.

(40) Sanz-Paz, M.; van Zanten, T. S.; Manzo, C.; Mivelle, M.; Garcia-Parajo, M. F. Broadband Plasmonic Nanoantennas for Multi-Color Nanoscale Dynamics in Living Cells. *Small* **2023**, *19*, 2207977.

(41) Taminiau, T. H.; Stefani, F. D.; Segerink, F. B.; van Hulst, N. F. Optical antennas direct single-molecule emission. *Nat. Photonics* **2008**, *2*, 234−237.

(42) Oulton, R. F.; Sorger, V. J.; Zentgraf, T.; Ma, R.-M.; Gladden, C.; Dai, L.; Bartal, G.; Zhang, X. Plasmon lasers at deep subwavelength scale. *Nature* **2009**, *461*, 629−632.

(43) Albrechtsen, M.; Vosoughi Lahijani, B.; Christiansen, R. E.; Nguyen, V. T. H.; Casses, L. N.; Hansen, S. E.; Stenger, N.; Sigmund, O.; Jansen, H.; Mørk, J.; Stobbe, S. Nanometer-scale photon confinement in topology-optimized dielectric cavities. *Nat. Commun.* **2022**, *13*, 6281.

(44) Navarro-Cia, M.; Maier, S. A. Broad-Band Near-Infrared Plasmonic Nanoantennas for Higher Harmonic Generation. *ACS Nano* **2012**, *6*, 3537−3544.

(45) Duarte, F.; Torres, J. P. N.; Baptista, A.; Marques Lameirinhas, R. A. Optical Nanoantennas for Photovoltaic Applications. *Nanomaterials* **2021**, *11*, 422.

(46) Hassan, E.; Evlyukhin, A. B.; Calà Lesina, A.. Anapole plasmonic meta-atom enabled by inverse design for metamaterials transparency. arXiv: 2303.00478v1, 2023; https://arxiv.org/abs/2303.00478, accessed on March 1, 2023.

(47) Gustavsen, B.; Semlyen, A. Rational approximation of frequency domain responses by vector fitting. *IEEE Trans. Power Deliv.* **1999**, *14*, 1052−1061.

(48) Liu, D.; Michalski, K. A. Comparative study of bio-inspired optimization algorithms and their application to dielectric function fitting. *J. Electromagn. Waves Appl.* **2016**, *30*, 1885−1894.

(49) Garcia-Vergara, M.; Demésy, G.; Zolla, F. Extracting an accurate model for permittivity from experimental data: hunting complex poles from the real line. *Opt. Lett.* **2017**, *42*, 1145−1148.

(50) Rakić, A. D. Algorithm for the determination of intrinsic optical constants of metal films: application to aluminum. *Appl. Opt.* **1995**, *34*, 4755−4767.

(51) Johnson, P. B.; Christy, R. W. Optical Constants of the Noble Metals. *Phys. Rev. B: Solid State* **1972**, *6*, 4370−4379.

(52) Schinke, C.; Peest, C.; Schmidt, J.; Brendel, R.; Vogt, M. R.; Kröger, I.; Winter, S.; Schirmacher, A.; Lim, S.; Nguyen, H.; Macdonald, D. Uncertainty analysis for the coefficient of band-to-band absorption of crystalline silicon. *AIP Adv.* **2015**, *5*, 067168.

(53) DeVore, J. R. Refractive Indices of Rutile and Sphalerite. *J. Opt. Soc. Am.* **1951**, *41*, 416−419.

(54) Vaccari, A.; Calà Lesina, A.; Cristoforetti, L.; Pontalti, R. Parallel implementation of a 3D subgridding FDTD algorithm for large simulations. *Prog. Electromagn. Res.* **2011**, *120*, 263−292.

(55) Aage, N.; Andreassen, E.; Lazarov, B. Topology optimization using PETSc: An easy-to-use, fully parallel, open source topology optimization framework. *Struct. Multidiscipl. Optim.* **2015**, *51*, 565−572.

(56) Wang, S.; Wu, P. C.; Su, V. C.; Lai, Y. C.; Chen, M. K.; Kuo, H. Y.; Chen, B. H.; Chen, Y. H.; Huang, T. T.; Wang, J. H.; et al. A broadband achromatic metalens in the visible. *Nat. Nanotechnol.* **2018**, *13*, 227−232.

(57) Hassan, E.; Wadbro, E.; Berggren, M. *Time-Domain Sensitivity Analysis for Conductivity Distribution in Maxwell's Equations*; Dept. of Computing Science, Umeå University, 2015.

(58) Yee, K.; Chen, J. The finite-difference time-domain (FDTD) and the finite-volume time-domain (FVTD) methods in solving Maxwell's equations. *IEEE Trans. Antennas Propag.* **1997**, *45*, 354−363.

(59) Bruns, T. E.; Tortorelli, D. A. Topology optimization of non-linear elastic structures and compliant mechanisms. *Comput. Methods Appl. Mech. Eng.* **2001**, *190*, 3443−3459.

(60) Bourdin, B. Filters in topology optimization. *Int. J. Numer. Methods Eng.* **2001**, *50*, 2143−2158.

(61) Hassan, E.; Wadbro, E.; Berggren, M. Patch and ground plane design of microstrip antennas by material distribution topology optimization. *Prog. Electromagn. Res. B* **2014**, *59*, 89−102.

(62) Aage, N.; Egede Johansen, V. Topology optimization of microwave waveguide filters. *Int. J. Numer. Methods Eng.* **2017**, *112*, 283−300.

(63) Sigmund, O. Morphology-based black and white filters for topology optimization. *Struct. Multidiscip. Optim.* **2007**, *33*, 401−424.

(64) Svanberg, K. The method of moving asymptotes—a new method for structural optimization. *Int. J. Numer. Methods Eng.* **1987**, *24*, 359−373.

(65) Li, L.; Wei, B.; Yang, Q.; Ge, D. Auxiliary differential equation finite-element time-domain method for electromagnetic analysis of dispersive media. *Optik* **2019**, *184*, 189−196.